Food Research International 222 (2025) 117734

Contents lists available at ScienceDirect

Food Research International

journal homepage: www.elsevier.com/locate/foodres

From emulsion to 3D-structurable oleogels: A hot-air drying strategy for plant-based fat systems with high oil content

Tao Wang [a,b], Manman Shi [a,b], Jun Cao [a,b], Pengfei Yu [c], Fuliang Cao [a], Erzheng Su [a,b,*]

[a] Co-innovation Center for the Sustainable Forestry in Southern China, State Key Laboratory for Development and Utilization of Forest Food Resources, Nanjing Forestry University, Nanjing 210037, China
[b] Department of Food Science and Engineering, College of Light Industry and Food Engineering, Nanjing Forestry University, Nanjing 210037, China
[c] Suining County Runqi Investment Co., Ltd, Xuzhou 221225, China

ARTICLE INFO

Keywords:
Plant-based oleogel
Protein-polysaccharide conjugates
3D printing
Solid fat replacement
Emulsion-templated gelation

ABSTRACT

Developing structured lipid systems with high oil content and functional applicability is critical for advancing next-generation clean-label and health-oriented food products. In this study, soy protein isolate (SPI) and sodium alginate (SA) were conjugated via pH-regulated Maillard glycation and used as emulsifiers to stabilize high internal phase emulsions (HIPEs). The emulsions, containing up to 75% (v/v) soybean oil, were transformed into oleogels using a solvent-free, energy-efficient hot-air drying process. The resulting oleogels exhibited real oil contents as high as 78.3%, with well-developed weak-gel rheological behavior, excellent oil-holding capacity, and desirable textural characteristics. Notably, oleogels with 70–75% oil content showed superior structural stability under ambient storage, thermal processing, and freeze–thaw conditions. In addition, the oleogels demonstrated good spreadability and 3D printability, indicating their suitability for application in advanced food structuring. These findings provide a sustainable and scalable approach for fabricating functional oleogels through the synergistic design of glycated biopolymer emulsifiers and mild drying techniques.

1. Introduction

In the food industry, solid fats are widely used to enhance product texture, flavor, and thermal stability. However, conventional solid fats are primarily derived from hydrogenated vegetable oils or animal fats and are rich in trans fatty acids (TFAs) and saturated fatty acids (SFAs). Long-term intake of these lipids is closely associated with health risks such as cardiovascular diseases (Li et al., 2022; Morales et al., 2023). As a result, developing healthy lipid substitutes based on polyunsaturated liquid vegetable oils has become a key direction in fat functionality research.

Oleogels are systems that convert liquid oils into semi-solid materials through the construction of three-dimensional networks. They confer solid fat-like processing and structural functionality to liquid oils, representing a promising strategy for healthy lipid replacement (Manzoor et al., 2022; Shuai et al., 2023). Compared with traditional approaches using high-melting-point waxes or crystalline fatty acids, the emulsion-template method is a solvent-free, gentle, and structurally tunable oleogel preparation technology that offers improved safety and industrial adaptability in food applications (Chen et al., 2025; Chen & Yang, 2019; Kavimughil et al., 2022; Tan et al., 2024; Wang et al., 2025; Xie et al., 2023). This method induces the formation of oil droplet networks via stabilized emulsion structures and is particularly suitable for constructing food-grade oleogels with high internal phase and high oil loading.

The key to constructing stable emulsion templates lies in emulsifier design. Protein–polysaccharide complexes are widely used in food interfacial material research due to their synergistic emulsification properties and film-forming capabilities. Among these, soy protein isolate (SPI) and sodium alginate (SA) are particularly attractive owing to their natural origin, amphiphilic structure, and electrostatic compatibility. In recent years, protein glycation modification has been proven to significantly enhance their structural flexibility and interfacial stability, making it an effective strategy for improving emulsion stability and gelation potential (Cai et al., 2018; Cui et al., 2023; Pan et al., 2021). However, the construction of high-oil oleogels that were previously difficult to obtain via emulsion-templated methods, whether SPI–SA conjugates can reliably stabilize high internal phase emulsions (HIPEs)

* Corresponding author at: Co-innovation Center for the Sustainable Forestry in Southern China, State Key Laboratory for Development and Utilization of Forest Food Resources, Nanjing Forestry University, Nanjing 210037, China.
E-mail addresses: taowang@njfu.edu.cn, ahzytaowang@163.com (T. Wang), ezhsu@njfu.edu.cn (E. Su).

https://doi.org/10.1016/j.foodres.2025.117734
Received 14 July 2025; Received in revised form 14 September 2025; Accepted 25 October 2025
Available online 29 October 2025

and subsequently form structurally coherent oleogels has not been systematically investigated. Furthermore, although freeze-drying is frequently employed to induce emulsion-to-gel transitions, the resulting gels are often rigid and brittle, limiting their applicability in spreadable or printed food systems (Abdolmaleki et al., 2020; Plazzotta et al., 2020). In contrast, hot-air drying offers a continuous, energy-efficient, and solvent-free alternative that is more compatible with large-scale food manufacturing (Moradabbasi et al., 2022). The thermal profile and gradual moisture removal characteristic of hot-air drying may facilitate the development of more cohesive and deformable oleogel networks. However, despite its industrial feasibility, whether hot-air drying can yield oleogels that simultaneously maintain structural integrity and application-relevant functionality (e.g., spreadability or 3D shape retention) remains poorly understood, and systematic studies in this context are lacking.

Based on these considerations, SPI–SA conjugates were selected as stabilizers because SPI provides amphiphilic interfacial activity while SA contributes hydrophilicity and structural support; after Maillard-type glycation, their combination enhances emulsion stability, reduces oil leakage, and facilitates the construction of high-oil oleogels with good integrity. It is hypothesized that SPI–SA conjugates obtained via pH-regulated glycation can effectively stabilize HIPEs, and that subsequent hot-air drying can convert these emulsions into structurally robust and functionally adaptable oleogels. The resulting oleogels, particularly at higher oil contents, are expected to exhibit improved oil-holding capacity, structural integrity, and desirable functional characteristics such as spreadability and 3D shape retention.

To evaluate this hypothesis, a pH-regulated glycated SPI–SA conjugate system was employed to stabilize high-oil emulsions, which were subsequently transformed into oleogels via hot-air drying. The resulting oleogels were systematically characterized for their rheological properties, textural behavior, structural stability, and functional performance, including 3D shape fidelity. This strategy offers a practical and scalable route for developing high-oil, plant-based oleogels suitable for food structuring and solid fat replacement.

2. Materials and methods

2.1. Materials

SA, SPI, o-phthaldialdehyde (OPA), and L-lysine were purchased from Shanghai Titan Scientific Co., Ltd. (Shanghai, China). Nile red was obtained from Nanjing Dolai Biotechnology Co., Ltd. (Nanjing, China), and fluorescein isothiocyanate (FITC) was purchased from Shanghai Macklin Biochemical Co., Ltd. (Shanghai, China). Soybean oil was obtained from COFCO Donghai Grain and Oil Industry Co., Ltd. (Zhangjiagang, China). All other reagents were of analytical grade and used as received without further purification.

2.2. Preparation of SPI–SA conjugates

The method was adapted from the reported protocol with some modifications (Hao et al., 2020; Kutzli et al., 2018; Peng et al., 2018; Zhu et al., 2023). SA (final concentration 0.5%, w/w) and SPI (final concentration 5%, w/w) were dissolved in sodium phosphate buffer (pH 6.8) under magnetic stirring at 1000 rpm for 6 h to ensure complete dissolution. The resulting mixture was then adjusted to pH 3.0, 5.0, 7.0, or 9.0, and incubated overnight at 4 °C. Subsequently, the solutions were incubated in a water bath at 70 °C for 36 h to induce glycation. After incubation, the pH of each solution was readjusted to its original value to obtain the SPI–SA conjugates.

2.3. Characterization of SPI–SA conjugates

2.3.1. Surface wettability

Powder samples were compressed into discs (10 mm diameter) at 20 MPa using a tablet press. The static contact angle was measured with a contact angle analyzer (LSA 100, LAUDA Scientific GmbH, Germany). A 3 μL droplet of deionized water was deposited onto the sample surface using a microsyringe, and the contact angle was automatically determined by the instrument software. All measurements were performed in triplicate.

2.3.2. Average particle size and zeta potential of the conjugates

The average particle size and zeta potential of the particle dispersions were measured using a Malvern Zetasizer Nano ZS (Malvern Instruments, UK). Prior to analysis, 1 mL of each sample was diluted 100-fold with deionized water. All measurements were conducted at 25 °C.

2.3.3. Degree of grafting and browning index of the conjugates

The browning index (BI) was determined at 420 nm using a modified version of the reported method (Lertittikul et al., 2007). Prior to measurement, the SPI–SA conjugate solution was diluted with distilled water to a final concentration of 5 mg/mL. The degree of grafting (DG) of the SPI–SA conjugates was quantified using the OPA method (Dinnella et al., 2002). The OPA reagent was prepared by dissolving 40 mg OPA in 1 mL methanol, followed by the addition of 25 mL of 0.1 M sodium borate buffer (pH 9.85), 100 μL β-mercaptoethanol, and 2.5 mL of 20% (w/v) sodium dodecyl sulfate (SDS). Deionized water was then added to reach a final volume of 50 mL. For analysis, 4 mL of OPA reagent was mixed with 200 μL of the sample solution in a test tube and incubated at 35 °C for 2 min. The absorbance was recorded at 340 nm using a UV–visible spectrophotometer. A standard curve was generated using L-lysine solutions at concentrations ranging from 0.5 to 3 mM.

The degree of glycation (DG) of the SPI–SA conjugates was determined according to Eq. (1):

$$DG(\%) = \left(\frac{C_1 - C_t}{C_1}\right) \times 100 \tag{1}$$

where C_1 and C_t represent the free amino group content in the mixture before and after the Maillard reaction, respectively.

2.3.4. Emulsifying activity and stability

The emulsifying activity (EAI) and emulsion stability (ESI) of the SPI–SA conjugates were determined using a turbidimetric method as previously described (Chen & Zhang, 2023; Yi et al., 2024; Zhang et al., 2024; Zhang, Zhang, et al., 2021). Briefly, 5 mL of soybean oil was mixed with 20 mL of a 0.1% (w/v) sample solution and homogenized at 12,000 rpm for 3 min using a high-speed homogenizer to prepare the emulsion. A 100 μL aliquot of the fresh emulsion was diluted in 9.9 mL of 0.1% (w/v) SDS solution. The emulsifying activity and stability were subsequently calculated using Eqs. (2) and (3):

$$EAI\ (m^2/g) = \frac{2 \times 2.303 \times A_0 \times D}{C \times V \times W \times 10^4} \tag{2}$$

$$ESI\ (min) = \frac{A_0 \times 15}{A_0 - A_{15}} \tag{3}$$

where A_0 and A_{15} represent the absorbance of the emulsion at 500 nm measured at 0 and 15 min, respectively. D is the dilution factor ($D = 100$), C is the protein concentration (g/mL), V is the volume fraction of oil in the emulsion ($V = 0.2$), and W is the path length of the cuvette ($W = 0.01$ m).

2.3.5. Fourier transform infrared (FTIR) spectroscopy

Freeze-dried powders of SPI–SA conjugates prepared at different pH values (3.0, 5.0, 7.0, and 9.0) were used for FTIR analysis. The samples were thoroughly ground and mixed with spectroscopic-grade potassium bromide (KBr) at a ratio of 1:100 (w/w), and then compressed into transparent pellets using a hydraulic press. FTIR spectra were acquired using a spectrometer (Nicolet iS10, Thermo Fisher Scientific, USA) over

the range of 4000–400 cm^{-1}, with a resolution of 4 cm^{-1} and 32 scans per sample, as described by Chen et al. (2023).

2.4. Preparation of SPI–SA-based oleogels via emulsion templating and hot-air drying

Oleogel preparation was carried out according to the reported method, with some modifications to suit the experimental conditions (Chen & Yang, 2019; Miao et al., 2025). Soybean oil was incorporated into the glycated SPI–SA conjugate solutions (5.5%, w/w) at final concentrations of 40%, 55%, 70%, and 75% (v/v). The mixtures were homogenized at 12,000 rpm for 2 min using a high-speed homogenizer to form fresh emulsions. The emulsions were then transferred into flat petri dishes and subjected to hot-air drying at 45 °C for 24 h. This process induced structural gelation of the emulsion, yielding SPI–SA-based oleogels with varying oil contents. Following drying, the actual oil content of the resulting oleogels was recalculated based on gravimetrically determined residual moisture and initial emulsion oil volume. Assuming an oil density of 0.92 g/mL, the true oil content of the dried oleogels was estimated to be 64.78%, 71.00%, 75.22%, and 78.34% for the 40%, 55%, 70%, and 75% formulations, respectively. The oleogels were collected and stored at room temperature (~25 °C) for further characterization.

2.5. Characterization of emulsions and oleogels

2.5.1. Average droplet size and zeta potential of emulsions

The method was the same as described in Section 2.3.2.

2.5.2. Confocal laser scanning microscopy (CLSM)

To visualize the internal network structure of the emulsion and oleogel, the oil phase was stained with Nile red and the aqueous phase with FITC. The samples were then imaged using a CLSM (LSM 900, ZEISS, Germany) under 565 nm and 488 nm excitation, respectively.

2.5.3. Centrifugal stability

To evaluate centrifugal stability, the freshly prepared emulsions were centrifuged at 5000 rpm for 30 min. The centrifugal stability (%) was calculated according to Eq. (4):

$$\text{Centrifugal stability}\ (\%) = \frac{w_0 - w_1}{w_0} \times 100 \quad (4)$$

where w_0 is the total mass of the emulsion before centrifugation, and w_1 is the mass of the remaining gel-like phase after removal of the separated water and oil.

2.5.4. Rheological characterization of emulsions and oleogels

The rheological properties of emulsions and oleogels were measured using a rotational rheometer (MARS60, Thermofisher Scientific, Germany) equipped with a 40 mm parallel plate geometry and a fixed gap of 1 mm. All measurements were performed at 25.0 ± 0.1 °C, and samples were allowed to equilibrate on the plate for 1 min before testing.

To identify the linear viscoelastic region (LVR), a strain sweep was first conducted at a constant frequency of 1 Hz over a strain range of 0.1% to 100%. All subsequent dynamic measurements were performed within the LVR.

For steady shear measurements, the apparent viscosity of the emulsions and oleogels was recorded over a shear rate range of 0.1 to 100 s^{-1}.

For frequency sweep tests, the storage modulus (G′) and loss modulus (G″) were determined over a frequency range of 1–10 Hz at a constant strain of 0.1% (within the LVR).

For creep–recovery tests, a constant shear stress of 100 μN/m^2 was applied to the oleogel samples for 2 min to monitor time-dependent deformation (creep phase), followed by stress removal and a 2 min observation of recovery behavior.

For temperature ramp tests, the G′ and G″ of oleogels were recorded during a controlled heating–cooling cycle: the temperature was increased from 25 °C to 80 °C, held at 80 °C for 5 min, and then decreased back to 25 °C.

2.5.5. Oil loss measurement of oleogels during ambient storage

The oil-holding capacity of oleogels under ambient conditions was evaluated by monitoring oil loss over a 7-day period at room temperature (~25 °C). Freshly prepared oleogels were placed in petri dishes and stored undisturbed. Every 24 h, the released oil on the surface was carefully removed using filter paper and weighed. The relative oil release rate (%) was calculated based on the initial mass of the oleogel according to Eq. (5):

$$\text{Oil release rate}\ (\%) = (W_r/Wi) \times 100 \quad (5)$$

where W_r is the cumulative weight of the oil released at each time point, and Wi is the initial weight of the oleogel sample.

2.5.6. Oil loss measurement of oleogels under heating conditions

The thermal oil-holding capacity of the oleogels was assessed by quantifying oil loss during heating at 60 °C over an 8 h period. Oleogel samples were placed in petri dishes and transferred to a constant-temperature oven set at 60 °C. At 2 h intervals (0, 2, 4, 6, and 8 h), the released surface oil was gently removed and weighed. After each measurement, samples were returned to the oven for continued incubation.

The oil holding capacity (%) was calculated relative to the initial mass of the oleogel according to Eq. (6):

$$\text{Oil holding capacity}\ (\%) = \left(1 - \frac{W_o}{Wg}\right) \times 100 \quad (6)$$

where W_o is the cumulative weight of oil released at each time point, and Wg is the initial weight of the oleogel.

2.5.7. Freeze-thaw stability of oleogels

The freeze–thaw stability of the oleogels was evaluated over five complete cycles. In each cycle, samples were stored at −20 °C for 18 h, followed by thawing at 25 °C for 6 h. After each cycle, the oil released from the surface of the oleogel was gently removed and weighed.

The oil loss (%) for each cycle was calculated according to Eq. (7):

$$\text{Oil holding capacity}\ (\%) = \left(1 - \frac{W_f}{Wo}\right) \times 100 \quad (7)$$

where W_f is the weight of oil released after each freeze–thaw cycle, and Wo is the initial weight of the oleogel sample.

2.5.8. Texture profile analysis (TPA) of oleogels

The textural properties of the oleogels were assessed using a texture analyzer (Stable Micro Systems Co. Ltd., Godalming, UK) operating in TPA mode. A cylindrical probe (P/0.5) was used, and samples were equilibrated to room temperature (~25 °C) prior to testing. The pre-test, test, and post-test speeds were each set to 1.0 mm/s, with a compression depth of 3 mm. Measurements were conducted at room temperature, and each sample group was tested in triplicate to obtain hardness, cohesiveness, springiness, and chewiness parameters.

2.6. Spreadability measurement of oleogels

The spreadability of the oleogels was determined using a modified parallel-plate method as previously described by Erum et al. (2024) and Abdallah et al. (2021), with slight modifications. Briefy, approximately 1.0 g of oleogel sample was placed between two parallel glass plates (10 cm × 10 cm), and a standard weight (typically 500 g) was gently placed on the upper plate. After 60 s, the diameter of the spread area was

measured in two perpendicular directions and averaged. The spreadability value was calculated according to Eq. (8):

$$Spreadability\ (g \bullet cm/s) = (m \times d)/t \quad (8)$$

where m is the applied weight (g), d is the average diameter of the spread area (cm), and t is the time allowed for spreading (s). All measurements were conducted at room temperature (~25 °C), and each test was performed in triplicate.

2.7. Assessment of 3D printing fidelity and structural stability of oleogels

To evaluate the printability and shape retention of oleogels, samples with different oil contents (40%, 55%, 70%, and 75%) were loaded into a syringe-based extrusion 3D printer (FOODBOT D1, Hangzhou Shiyin Technology Co., Ltd., China). A standardized model, a Mickey Mouse head (35 mm length × 30 mm width × 5 mm height), was printed onto a flat acrylic substrate under room temperature (~25 °C) condition. Each formulation was printed in triplicate.

Printing accuracy was assessed by measuring the actual length, width, and height of each printed structure using a digital caliper (precision ± 0.01 mm). The mean deviation from the target dimension was calculated for each axis and averaged to obtain the overall dimensional error. Accuracy (%) was then determined according to Eq. (9):

$$Accuracy\ (\%) = \left[1 - \left(\frac{|Measured - Design|}{Design}\right)\right] \times 100 \quad (9)$$

Printing stability was evaluated by monitoring shape deformation over 6 h at room temperature (~25 °C). Length, width, and height were recorded at 0, 2, 4, and 6 h. Shape retention was calculated based on dimensional change according to Eq. (10):

$$Stability\ (\%) = (Dimension\_t/Dimension_0) \times 100 \quad (10)$$

where $Dimension\_t$ is the length, width, or height at time t, and $Dimension_0$ is the initial printed dimension.

2.8. Statistical analysis

All experiments were conducted in triplicate, and the results are expressed as means ± standard deviations. Statistical significance was assessed using analysis of variance (ANOVA), followed by Waller-Duncan post hoc test. Differences were considered significant at $P < 0.05$. All statistical analyses were performed using SPSS software (version 20.0; SPSS Inc., Chicago, IL, USA), and data visualizations were generated with Origin 2024 (OriginLab Corp., Northampton, MA, USA).

3. Results and discussion

3.1. Structural and emulsifying characteristics of SPI–SA Maillard conjugates prepared under different pH conditions

The SPI–SA conjugates exhibited significant variation in interfacial and structural properties with pH. As shown in Fig. 1B, conjugates prepared at pH 9 showed the smallest mean particle size (~2.7 μm), which is advantageous for emulsion stability due to a higher surface area facilitating rapid interfacial adsorption. Although the zeta potential at pH 9 (−28.2 mV) was not the most negative among all groups, it remained within the effective electrostatic repulsion range for colloidal stability (typically −30 to −50 mV), aligning with reported findings that moderate surface charge combined with structural flexibility optimizes emulsion stabilization (Sun et al., 2022). By contrast, the non-glycated SPI–SA complexes at pH 9 exhibited a comparable zeta potential (around −28.9 mV) but a larger particle size (~3.6 μm) (Fig. 1A). These results suggest that while both systems provided sufficient electrostatic repulsion, glycation substantially reduced particle size and enhanced interfacial adsorption.

The DG and BI also peaked under pH 9 (Fig. 1C), suggesting enhanced Maillard reactivity. The DG (~31.5%) at pH 9 falls within the

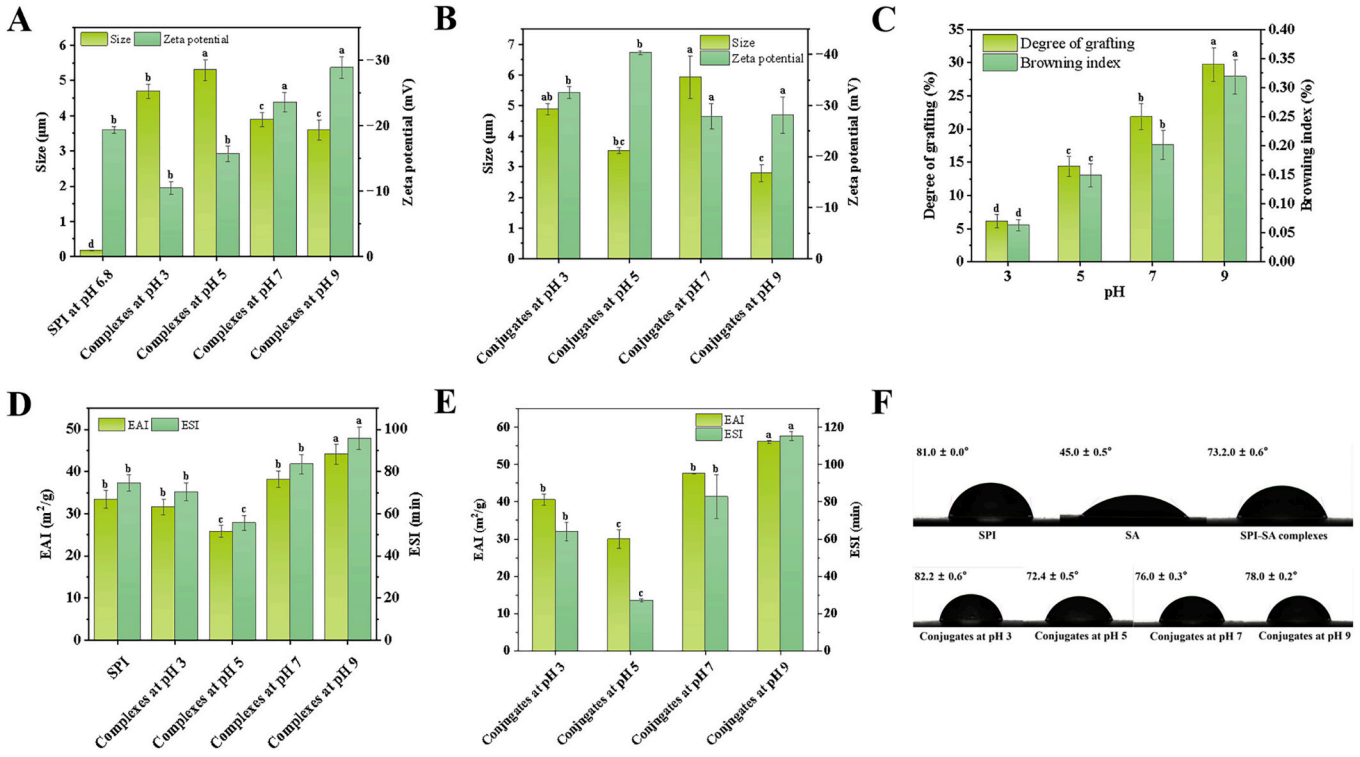

Fig. 1. (A) Average particle size and zeta potential of SPI and SPI–SA complexes. (B) Average particle size and zeta potential of SPI–SA conjugates. (C) Degree of grafting and browning index of SPI–SA conjugates. (D) EAI and ESI of SPI and SPI–SA complexes. (E) EAI and ESI of SPI–SA conjugates. (F) Contact angles. Different letters indicate significant differences ($P < 0.05$).

optimal range (30–50%) for functional modification without excessive protein cross-linking or polymerization, which can otherwise impair solubility and emulsification (Kusumastuti et al., 2024; Tao et al., 2024). Moderate browning, as indicated by the BI, suggests that the conjugation process remained controlled, consistent with effective Maillard conjugation without overreaction.

In terms of emulsification, the pH 9 conjugate exhibited the highest emulsifying activity index (EAI = 56.2 m^2/g) and emulsion stability index (ESI = 115.3 min) (Fig. 1E). These values are notably higher than those reported for other SPI-based conjugates such as SPI–pectin (EAI ~49.8 m^2/g) (Ma et al., 2022), SPI–ginseng polysaccharide (EAI ~31.3 m^2/g) (Tao et al., 2024), and enzymatically hydrolyzed SPI–sugar conjugate system (EAI 44.6 m^2/g) (Wang et al., 2019). The combination of fine particle size, optimal charge, and high DG likely synergistically enhanced interfacial film formation and viscoelastic stabilization, consistent with the hypothesis that moderate glycation improves emulsifier flexibility and surface activity without causing excessive insolubility (Sun et al., 2022). In comparison, the non-glycated SPI–SA complexes at pH 9 showed lower EAI and ESI values, further confirming that glycation substantially improved the emulsifying capacity of SPI–SA systems.

The contact angle measurements (Fig. 1F; SPI: 81°, SA: 45°; non-glycated SPI–SA complexes: 73.3°; glycated SPI–SA conjugates: 82.2° at pH 3, 72.4° at pH 5, 76.0° at pH 7, 78.2° at pH 9) indicate intermediate wettability (60–90°), characteristic of Pickering particles (Wang et al., 2024). These results suggest that SPI–SA conjugates can serve as Pickering-type stabilizers, while still retaining protein–polysaccharide interfacial activity.

Taken together, the SPI–SA conjugates prepared at pH 9 exhibit the most favorable balance of physicochemical and interfacial properties. Their superior emulsifying performance and stability indicate that they provide a suitable foundation for further applications in HIPEs and oleogel structuring.

3.2. FTIR spectroscopy

FTIR spectroscopy was applied to characterize the structural changes of SPI–SA conjugates prepared at pH 3, 5, 7, and 9, in order to assess the extent of Maillard-type glycation (Fig. 2). Across all samples, a broad absorption band at 3200–3400 cm^{-1}, corresponding to the stretching vibrations of O—H and N—H groups, was observed. At pH 9, this band became broader and slightly less intense, suggesting stronger hydrogen bonding and possible consumption of free amino groups during conjugation, a pattern that has been linked to early-stage Maillard reactions in other protein–polysaccharide systems (Boonlao et al., 2023).

Changes in the amide I (~1650 cm^{-1}, C═O stretching) and amide II (~1550 cm^{-1}, N—H bending) bands were also observed, especially in the pH 9 sample. The slight shift and reduced intensity of these peaks are indicative of alterations in the protein secondary structure, likely caused by the formation of covalent bonds between the amino groups of SPI and the carbonyl groups of SA. These spectral features are consistent with previous FTIR characterizations of Maillard-conjugated protein–polysaccharide conjugates (Hussain et al., 2024; Li, Huang, et al., 2025).

Furthermore, increased intensity in the 1030–1070 cm^{-1} region, associated with C–O–C stretching of glycosidic bonds, was more pronounced in the pH 9 conjugate, supporting the hypothesis that more sugar residues were successfully grafted. Combined with the highest DG (32.5%) and BI observed at this pH, these spectral trends confirm that Maillard reactions proceeded more efficiently under mildly alkaline conditions.

Overall, the FTIR results provide molecular-level evidence that glycation between SPI and SA was more extensive at pH 9. These findings support the selection of the pH 9 conjugate as the optimal emulsifier precursor in subsequent HIPE and oleogel fabrication.

3.3. Physicochemical stability of emulsions

The physicochemical stability of emulsions plays a critical role in determining their suitability for downstream processing into oleogel

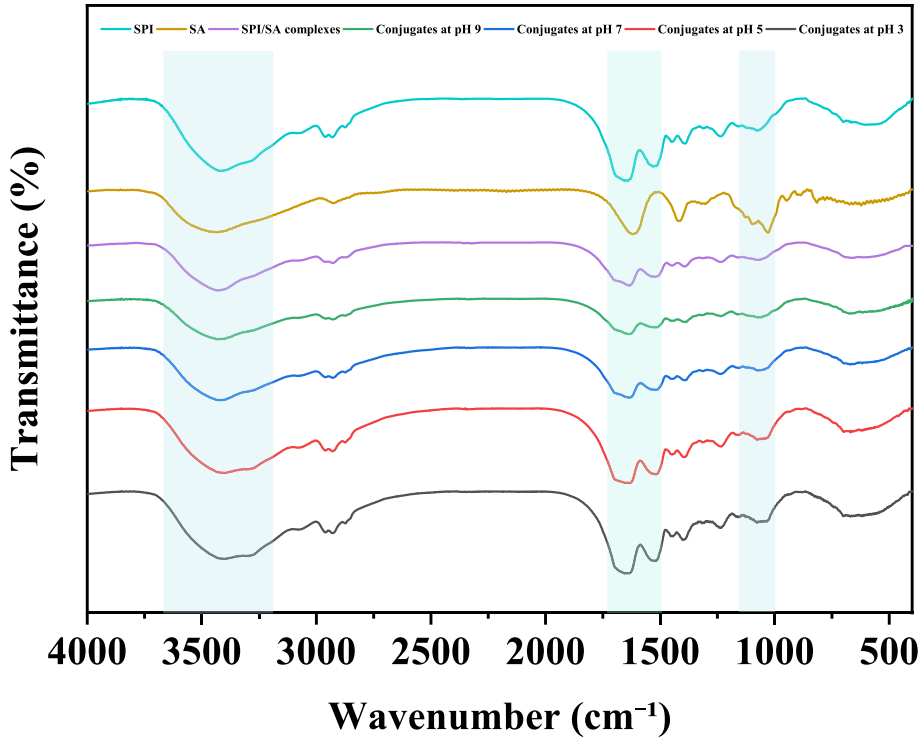

Fig. 2. FTIR spectra.

systems. Here, we systematically evaluated the impact of oil content (40–75%) on droplet size, zeta potential, and centrifugal stability of SPI–SA-based emulsions (Fig. 3).

As the oil content increased from 40% to 75%, a progressive increase in average droplet size was observed (from ~2.6 μm to ~6.9 μm). This trend aligns with classical emulsion theory: at higher internal phase volume fractions, limited aqueous continuous phase and surfactant lead to less efficient oil droplet dispersion and larger droplet formation.

The zeta potential values ranged from −37.4 to −43.2 mV, with emulsions at 70% and 75% oil exhibiting the highest surface charge (−42.1 and −43.2 mV, respectively). These values surpass the −30 mV threshold commonly associated with electrostatic stabilization (Djerdjev & Beattie, 2008), suggesting robust repulsive forces between droplets and reduced aggregation risk. However, while smaller droplet size typically correlates with improved kinetic stability, the strong zeta potential of the larger-droplet emulsions at 70% and 75% may offset their size disadvantage by preventing coalescence.

Centrifugal testing revealed a significant increase in emulsion stability with higher oil content: from 85.2% at 40% to 98.4% at 75%. This result may be attributed to the transition into high internal phase emulsion (HIPE) regime (>74% oil), where densely packed droplets form a pseudo-solid network that resists phase separation under centrifugal force (Roland et al., 2003). Similar behavior has been reported in emulsions stabilized by polymeric interfaces or dense droplet packing, where structural rigidity compensates for lower aqueous phase mobility (Onaizi, 2022).

Interestingly, although the 40% emulsion showed the smallest droplet size, it had the weakest centrifugal stability. This supports findings by Carasso et al., who emphasized that surface charge magnitude, rather than droplet size alone, is a more reliable predictor of emulsion stability under stress (Carasso et al., 1995). Collectively, the data indicate that SPI–SA emulsions with 70–75% oil content strike a favorable balance between interfacial charge, droplet size, and mechanical stability. These attributes are essential for maintaining emulsion integrity during subsequent thermal drying, positioning these formulations as optimal templates for stable oleogel development.

3.4. Microstructure of emulsions and oleogels observed by CLSM

The microstructures of emulsions and the corresponding oleogels prepared with varying oil contents (40% to 75%) were visualized by CLSM (Fig. 4). As the oil content increased, striking differences in droplet morphology and spatial organization were observed, which directly relate to emulsion stability and suitability for oleogel formation.

In emulsions with lower oil contents (40% and 55%), oil droplets were mostly spherical, loosely distributed, and exhibited noticeable polydispersity. The inter-droplet spacing was large, and only partial interfacial coverage was observed under CLSM, suggesting a discontinuous network and limited steric stabilization. These characteristics imply lower physical stability and reduced resistance to structural rearrangement or coalescence during gelation or drying processes. Similar observations have been reported in emulsions stabilized with under-packed droplet phases (Zhang, Cheng, et al., 2021).

In contrast, the 70% and 75% emulsions displayed typical HIPE microstructures, featuring closely packed, often polygonal droplets with minimal continuous phase. The CLSM images revealed clear interfacial layers between neighboring droplets, forming a compact and jammed droplet network. These features are known to enhance emulsion stability by restricting droplet mobility and promoting gel-like rheological behavior (Leng et al., 2022).

The observed dense droplet packing and interfacial continuity in the 70% and 75% emulsions are consistent with their high ESI and low oil separation rate. Importantly, this spatial structure offers a favorable physical framework for the construction of self-supporting oleogels.

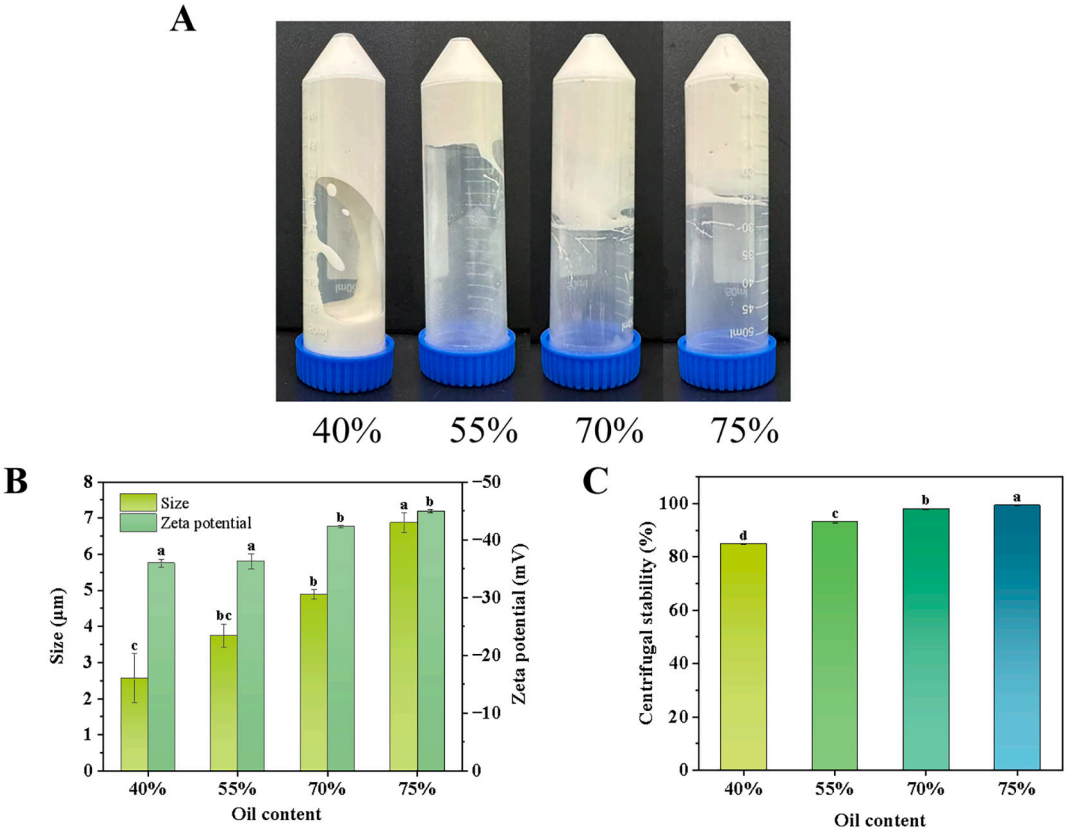

Fig. 3. (A) Inverted morphology of emulsions with different oil contents. (B) Average droplet size and zeta potential of emulsions with different oil contents. (C) Centrifugal stability of emulsions with different oil contents. Different letters represent a significant difference ($P < 0.05$).

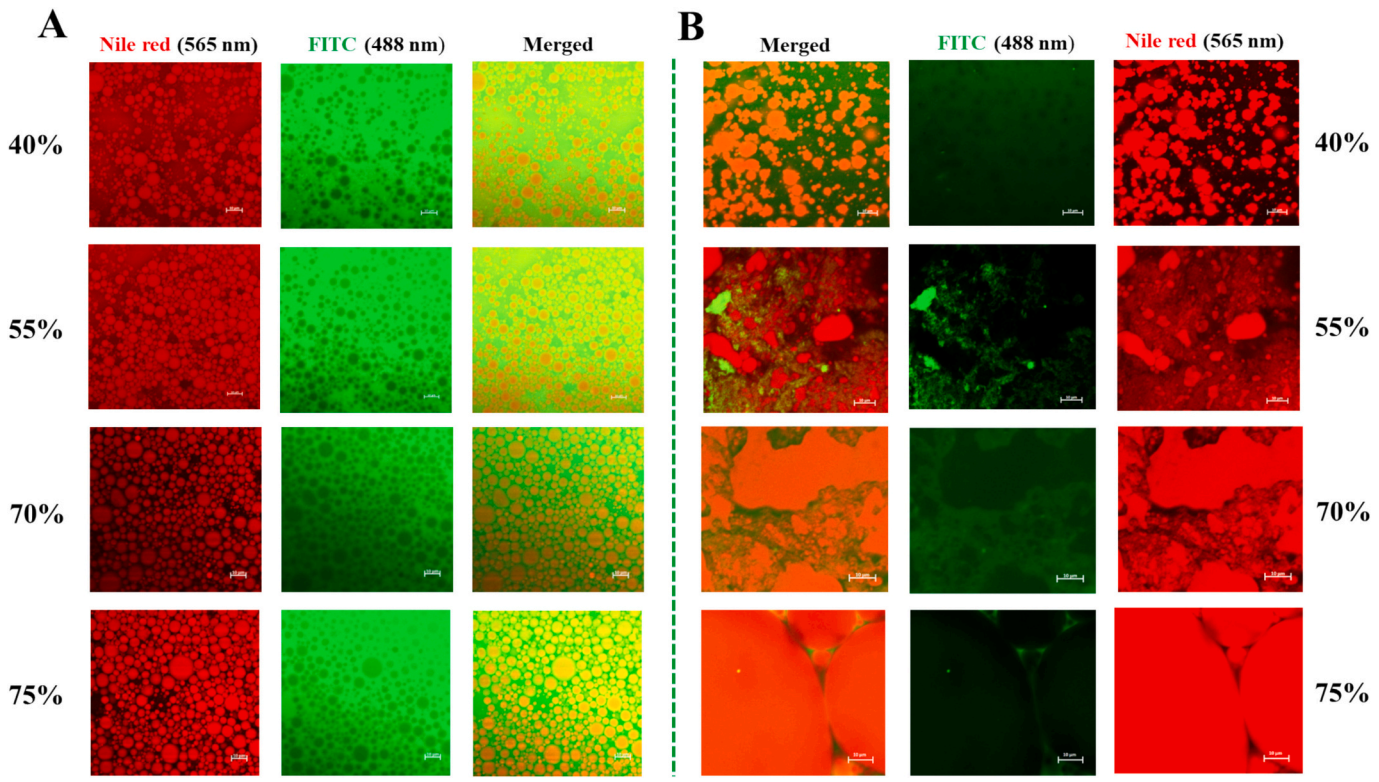

Fig. 4. CLSM images of emulsions (A) and oleogels (B) with different oil contents. Scale bar: 10 μm.

Previous studies have shown that emulsions with HIPE-like architectures serve as ideal templates for gelation due to their inherent viscoelasticity and minimal phase separation (Pan et al., 2025).

After hot-air drying, the emulsions transformed into oleogels with more compact and continuous networks, where oil droplets were closely packed and embedded within the SPI–SA matrix. At higher oil contents (70% and 75%), the oleogels exhibited a denser droplet network with reduced void spaces, indicating improved structural integrity and oil-holding capacity.

3.5. Rheological behavior of emulsions

The rheological profiles of emulsions with different oil contents (40%, 55%, 70%, 75%) were investigated through oscillatory frequency sweep and steady-state shear tests to evaluate their viscoelastic properties and shear behavior (Fig. 5). All emulsions exhibited solid-like viscoelastic behavior, with G′ consistently higher than G″ across the frequency range, and demonstrated shear-thinning behavior, characteristic of structured emulsions.

Specifically, G′ values increased significantly with oil content. At 75% oil loading, the emulsion exhibited the highest G′ ($>10^3$ Pa), suggesting enhanced structural integrity due to droplet crowding and jamming in HIPEs. This phenomenon aligns with previous findings indicating that increasing the dispersed phase volume enhances elastic modulus and yield stress due to droplet deformation and close packing (Pal, 2006).

The tan δ values (G″/G′) of emulsions with different oil contents (Table 1) further confirmed the dominance of elastic behavior in 70% and 75% emulsions, remaining below 0.15 across most frequencies, indicating strong gel-like characteristics desirable for oil gel precursor systems (Tripathi et al., 2017). In contrast, the 40% emulsion exhibited much lower G′ and higher tan δ, indicating a weaker structure with predominantly viscous behavior, unsuitable for further gel formation.

Steady shear tests (Fig. 5D) revealed that all samples displayed pronounced shear-thinning behavior, typical of structured emulsions. Viscosity dramatically decreased with increasing shear rate, particularly for the 70% and 75% systems. These emulsions also possessed the highest zero-shear viscosity, implying greater resistance to flow under low stress, a favorable attribute for structural stability and subsequent oil gelation (Welch et al., 2006).

Notably, the 70% emulsion showed a superior balance of elasticity, moderate viscosity, and low tan δ, this suggests that it combines structural rigidity with controllable flow behavior, both of which are beneficial for downstream oleogel processing. The 75% emulsion, although highly elastic and viscous, may be prone to slightly reduced homogeneity due to excessive internal phase crowding, potentially affecting surface smoothness after drying. This is consistent with reports that overly concentrated HIPEs may exhibit irregular microstructures or localized phase inversion when exceeding optimal packing limits (Ling et al., 2024; Zou et al., 2019).

3.6. Rheological evolution from emulsions to oleogels

To evaluate the mechanical performance of SPI–SA oleogels derived from high internal phase emulsions HIPEs, we conducted comprehensive rheological assessments including frequency sweep, shear flow, temperature ramp, and creep recovery tests (Fig. 6). The data revealed a consistent increase in viscoelastic properties with rising oil content (from 40% to 75%), indicating superior network integrity in high-oil formulations. This behavior aligns with recent studies demonstrating that oleogels with higher internal phase fractions typically show enhanced stiffness and stability due to tighter droplet packing and more continuous network formation (Shang et al., 2023).

The G′ and G″ of all samples were frequency-independent, suggesting solid-like gel behavior. Both G′ and G″ increased significantly with oil content. The 70% and 75% oleogels exhibited the highest G′ values (above 1000 Pa), reflecting robust network formation and structural rigidity. This trend mirrors observations in HIPE-derived oleogels where viscoelasticity improves due to the formation of a highly percolated droplet structure (Zheng et al., 2023).

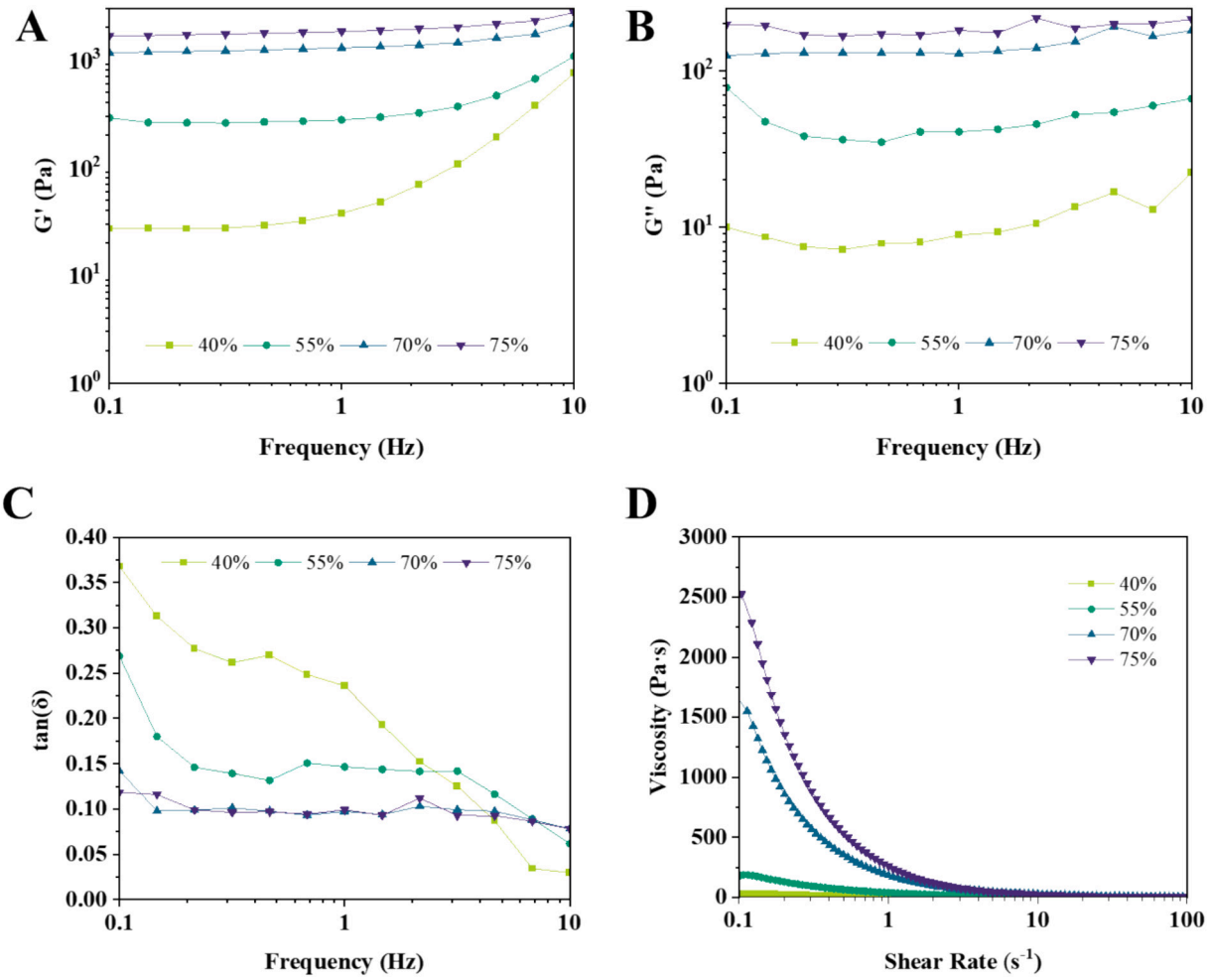

Fig. 5. Effect of oil content on the rheological behavior of emulsions. (A–C) Frequency sweep. (D) Apparent viscosity.

Moreover, the tan δ values of 70% and 75% oleogels (Table 2) remained below 0.15, indicating the dominance of elastic behavior. Such tan δ values are consistent with findings from Zhang et al. (2022), who reported that tan δ < 0.1 is characteristic of strong, weak gels with high deformation resistance.

All oleogels displayed typical shear-thinning behavior. Notably, 70% and 75% oleogels demonstrated the highest initial viscosity (>9000 Pa·s), with a steep decline under increasing shear rate, implying efficient structural breakdown under external stress. Such rheo-fluidifying characteristics are advantageous for applications requiring spreadability or extrusion (e.g., 3D printing), as highlighted by Wang, Huang, et al. (2023).

The creep-recovery tests indicated that the 70% and 75% oleogels had better recoverability, reflecting greater resistance to long-term deformation. Furthermore, during the temperature sweep (25 °C → 80 °C → 25 °C), 75% oleogels maintained a relatively high G′ throughout, indicating superior thermal robustness. Similar results were seen in caseinate- or polysaccharide-stabilized HIPE systems where high oil fractions conferred enhanced thermal stability through tightly packed droplet interfaces (Chen et al., 2017).

Compared to their precursor emulsions, the SPI–SA-based oleogels exhibited a marked transition in rheological behavior, characterized by a substantial increase in storage modulus, loss modulus, and apparent viscosity. For instance, at identical frequency and strain conditions, the G′ of 70% and 75% oil content oleogels increased by nearly an order of magnitude relative to their emulsion counterparts, indicating a denser and more elastic network structure. This enhancement is attributed to the water removal during drying, which facilitates droplet crowding and promotes the formation of a continuous inter-droplet protein–polysaccharide matrix. Similar gelation-enhancing effects upon emulsion dehydration have been reported in high internal phase systems stabilized by polysaccharide–protein complexes (Sun et al., 2023). Moreover, the reduction in tan δ values in the gels highlights a shift from predominantly viscoelastic to more elastic, solid-like behavior, critical for ensuring post-processing shape retention and mechanical stability.

3.7. Stability of SPI–SA oleogels under ambient, thermal, and freeze–thaw conditions

3.7.1. Room-temperature oil loss

The oil release behavior of oleogels over seven days at ambient storage revealed a clear oil content-dependent trend (Fig. 7). The 40% oil system exhibited a steep rise in oil release, reaching ~16% by day 7, whereas the 70% and 75% oleogels retained over 95% of oil content throughout. The enhanced oil-holding performance of higher oil content gels may be attributed to a denser droplet packing and a more continuous 3D network structure that restricts oil diffusion.

Similar results were reported by Zhang, Lu, et al. (2021), who demonstrated that increased internal phase fractions in oleogel-based HIPEs led to improved thermodynamic stability and suppressed oil migration during storage. This suggests that in our system, the SPI–SA-stabilized high internal phase structure provides robust interfacial resistance and capillary forces that hinder oil coalescence and leakage.

Table 1
Tan δ values of emulsions with different oil contents at various frequencies.

Frequency (Hz)	Oil content			
	40%	55%	70%	75%
0.10	0.267 ± 0.006^{a}	0.172 ± .0355^{a}	0.102 ± 0.003^{a}	0.097 ± 0.007^{a}
0.15	0.252 ± 0.021^{ab}	0.159 ± 0.013^{a}	0.099 ± 0.009^{a}	0.080 ± 0.007^{b}
0.22	0.217 ± 0.014^{c}	0.143 ± 0.010^{a}	0.071 ± 0.036^{ab}	0.078 ± 0.004^{b}
0.32	0.218 ± 0.005^{c}	0.148 ± 0.015^{a}	0.091 ± 0.003^{ab}	0.078 ± 0.003^{b}
0.464	0.235 ± 0.008^{bc}	0.147 ± 0.014^{a}	0.092 ± 0.001^{ab}	0.077 ± 0.009^{b}
0.68	0.232 ± 0.012^{bc}	0.153 ± 0.002^{a}	0.093 ± 0.007^{ab}	0.075 ± 0.003^{b}
1	0.236 ± 0.011^{bc}	0.157 ± 0.002^{a}	0.091 ± 0.001^{ab}	0.076 ± 0.001^{b}
1.47	0.216 ± 0.007^{c}	0.160 ± 0.002^{a}	0.091 ± 0.001^{ab}	0.078 ± 0.001^{b}
2.15	0.185 ± 0.009^{d}	0.161 ± 0.001^{a}	0.092 ± 0.004^{ab}	0.080 ± 0.002^{b}
3.16	0.169 ± 0.012^{d}	0.161 ± 0.001^{a}	0.093 ± 0.001^{ab}	0.082 ± 0.002^{b}
4.64	0.120 ± 0.008^{e}	0.149 ± 0.012^{a}	0.090 ± 0.003^{ab}	0.081 ± 0.002^{b}
6.81	0.078 ± 0.015^{f}	0.110 ± 0.017^{b}	0.084 ± .0065^{ab}	0.076 ± 0.008^{b}
10	0.030 ± 0.014^{g}	0.083 ± 0.013^{b}	0.064 ± 0.005^{b}	0.071 ± 0.007^{b}

Data are presented as mean ± SD. Different superscript letters within the same column indicate significant differences between groups ($P < 0.05$).

3.7.2. Thermal stability

Under accelerated thermal stress (60 °C), all oleogels showed some oil separation, but again, the 70% and 75% gels performed significantly better, with oil release remaining below 10% after 8 h (Fig. 8). This superior thermal stability likely arises from a combination of stronger viscoelasticity (Fig. 6D) and thermally resilient protein–polysaccharide interfacial layers.

Xu et al. (2024) found that reinforcing protein networks and interfacial film integrity in HIPEs substantially reduced thermally induced droplet coalescence and oil egress during heating cycles. Our data supports this conclusion, where the oil-retention efficiency at elevated temperatures increases with internal oil phase fraction.

3.7.3. Freeze-thaw stability

The freeze–thaw performance, evaluated over five cycles, again underscored the superiority of 70% and 75% oleogels (Fig. 9). These formulations retained more than 85% of their original oil after five

Table 2
Tan δ values of oleogels with different oil contents at various frequencies.

Frequency (Hz)	Oil content			
	40%	55%	70%	75%
0.10	0.192 ± 0.010^{ab}	0.179 ± 0.068^{a}	0.163 ± 0.044^{a}	0.127 ± 0.005^{a}
0.15	0.225 ± 0.048^{a}	0.134 ± 0.044^{ab}	0.108 ± 0.005^{b}	0.106 ± 0.015^{bcd}
0.22	0.184 ± 0.006^{b}	0.109 ± 0.013^{b}	0.103 ± 0.001^{b}	0.100 ± 0.006^{d}
0.32	0.162 ± 0.008^{b}	0.104 ± 0.004^{b}	0.102 ± 0.001^{b}	0.102 ± 0.007^{d}
0.464	0.161 ± 0.008^{b}	0.107 ± 0.011^{b}	0.100 ± 0.002^{b}	0.101 ± 0.005^{d}
0.68	0.159 ± 0.007^{b}	0.108 ± 0.011^{b}	0.117 ± 0.032^{b}	0.103 ± 0.004^{cd}
1	0.161 ± 0.009^{b}	0.102 ± 0.013^{b}	0.100 ± 0.003^{b}	0.106 ± 0.006^{cd}
1.47	0.163 ± 0.011^{b}	0.106 ± 0.012^{b}	0.103 ± 0.004^{b}	0.105 ± 0.006^{cd}
2.15	0.166 ± 0.004^{b}	0.114 ± 0.003^{ab}	0.105 ± 0.001^{b}	0.111 ± 0.002^{bcd}
3.16	0.172 ± 0.005^{b}	0.115 ± 0.006^{ab}	0.107 ± 0.001^{b}	0.115 ± 0.003^{abc}
4.64	0.179 ± 0.001^{b}	0.124 ± 0.005^{ab}	0.110 ± 0.004^{b}	0.120 ± 0.004^{ab}
6.81	0.175 ± 0.001^{b}	0.118 ± 0.012^{ab}	0.113 ± 0.003^{b}	0.122 ± 0.003^{ab}
10	0.167 ± 0.002^{b}	0.112 ± 0.003^{b}	0.109 ± 0.003^{b}	0.120 ± 0 .003^{ab}

Data are presented as mean ± SD. Different superscript letters within the same column indicate significant differences between groups ($P < 0.05$).

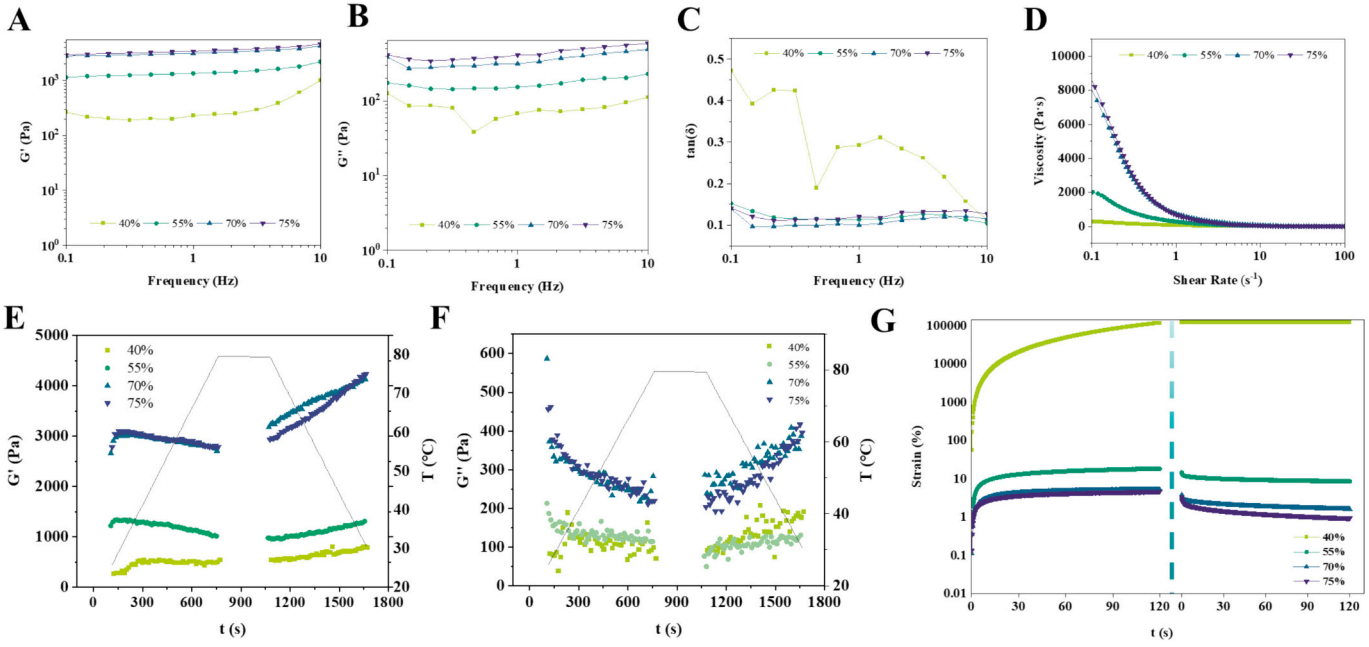

Fig. 6. Effect of oil content on the rheological behavior of oleogels. (A–C) Frequency sweep. (D) Apparent viscosity. (E–F) Temperature sweep. (G) Creep and recovery.

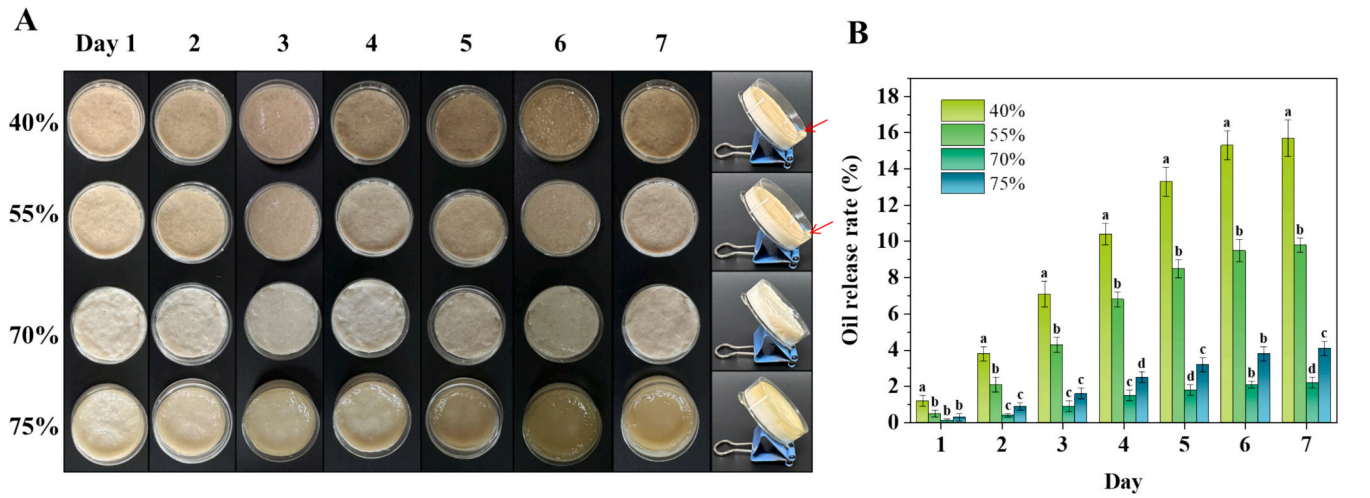

Fig. 7. Storage stability of oleogels at room temperature. (A) Visual appearance of oleogels after 7 days of storage. (B) Oil loss rate of oleogels during storage at room temperature. Different letters represent a significant difference ($P < 0.05$).

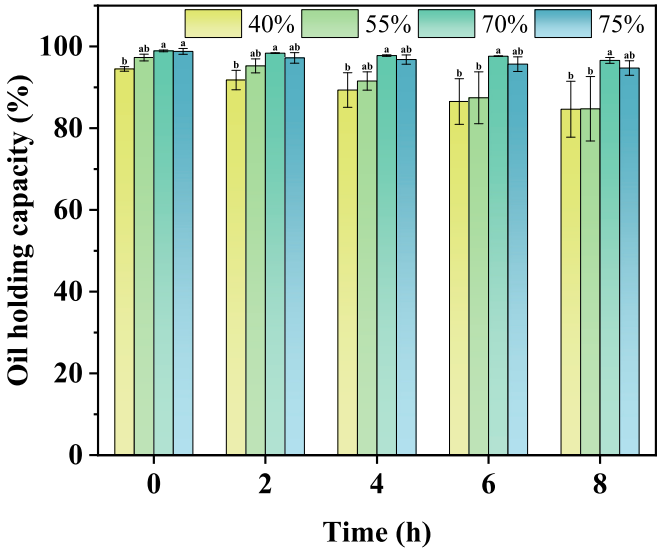

Fig. 8. Oil holding capacity of oleogels after heating. Different letters represent a significant difference ($P < 0.05$).

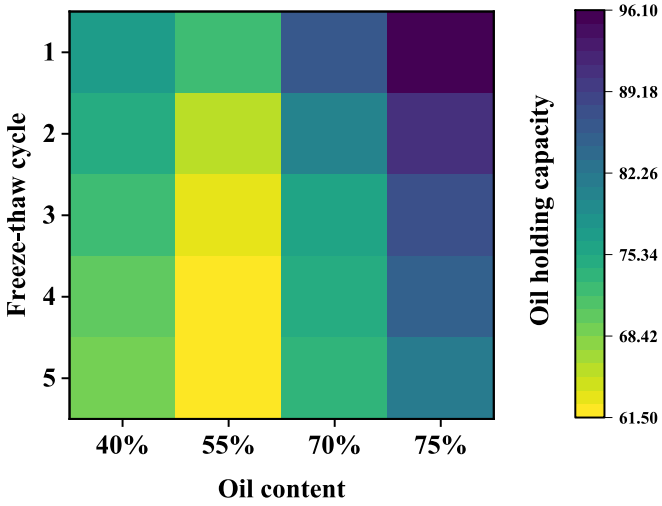

Fig. 9. Oil holding capacity of oleogels after five freeze–thaw cycles.

cycles, while the 40% system dropped below 70%. This can be attributed to the reduced free water and stronger network entrapment in high-oil gels, which minimized phase separation caused by ice crystal damage.

Li, Su, et al. (2025) reported that freeze–thaw resilience in HIPEs improved with increased internal oil fraction and robust interfacial assembly, which minimized structural breakdown upon ice melting. Similarly, Hu et al. (2023) showed that HIPEs with higher oil loadings preserved network integrity and volatile retention better over repeated freezing cycles.

Overall, the SPI–SA oleogels with 70% and 75% oil content demonstrate superior structural integrity and oil retention across diverse environmental stresses, underscoring their potential in applications requiring long-term and thermal stability.

These findings demonstrate that increasing oil content to 70–75% not only enhances the rheological properties of SPI–SA oleogels but also imparts superior stablity under ambient, thermal, and freeze–thaw conditions. This confirms the potential of high-oil HIPE-derived oleogels as robust fat alternatives for thermally or mechanically demanding food applications.

3.8. Textural properties of oleogels

Textural analysis revealed a consistent enhancement in mechanical robustness of SPI–SA oleogels with increasing oil content from 40% to 75% (Fig. 10A–F). Hardness, resilience, cohesiveness, gumminess, and chewiness all increased significantly with oil content ($P < 0.05$), suggesting that the higher oil fraction contributed to the formation of a more densely packed and structurally continuous gel network. The hardness rose from 30.4 g (40%) to 138.1 g (75%), and chewiness followed a similar trend, indicating stronger intermolecular interactions and a stiffer three-dimensional matrix as oil loading increased.

These results are consistent with previous findings demonstrating that elevated oil content within oleogel matrices can improve elasticity and firmness due to denser droplet packing and enhanced droplet–droplet interactions (Palla et al., 2017). In HIPEs, this behavior is attributed to the formation of a space-filling droplet network that transitions into a gel-like material upon dehydration (Wang, Jayani, et al., 2023).

Interestingly, springiness remained relatively stable across formulations (~80–85%), indicating that despite increased rigidity, the material maintained its ability to recover after deformation. This balance between firmness and elasticity is particularly relevant for applications requiring spreadability and shape retention, such as 3D printing or as functional lipid carriers in food matrices (Leahu et al., 2025).

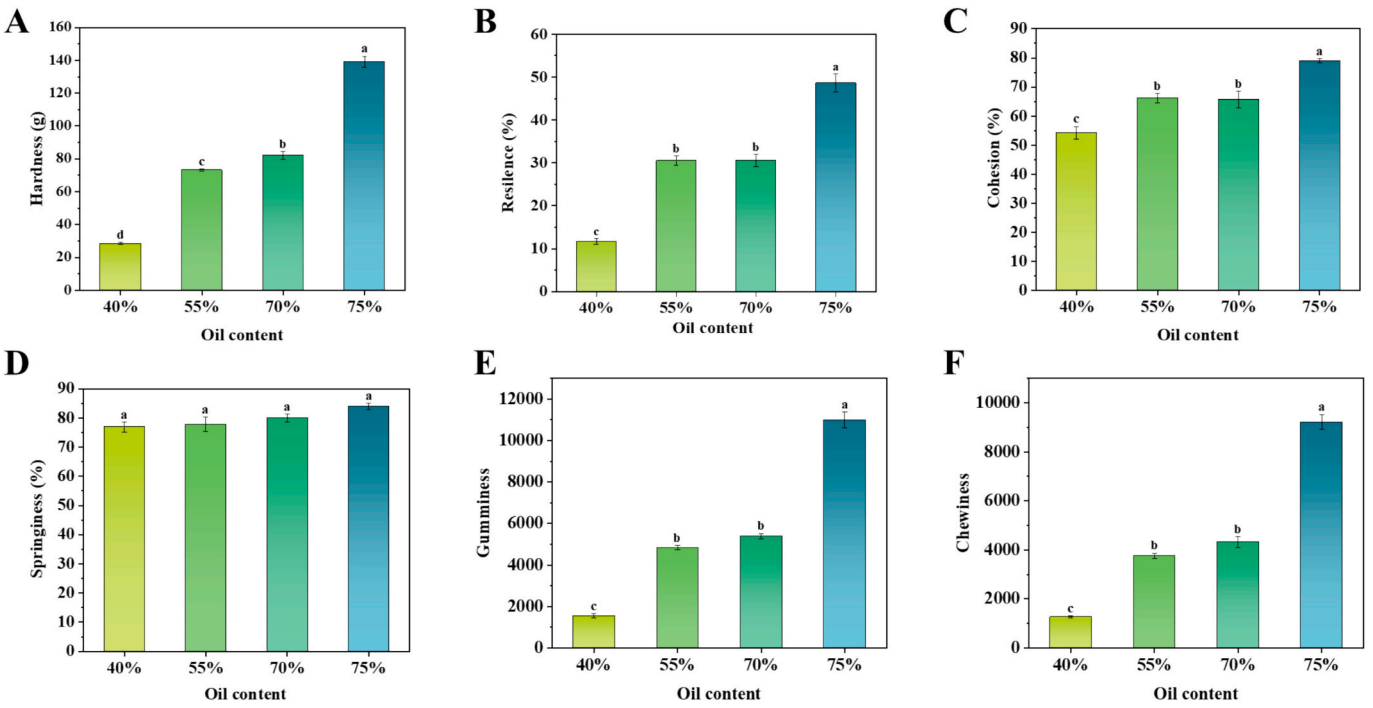

Fig. 10. Textural properties of oleogels. (A) Hardness. (B) Resilience. (C) Cohesiveness. (D) Springiness. (E) Gumminess. (F) Chewiness. Different letters represent a significant difference ($P < 0.05$).

The improved texture of the 70% and 75% oleogels correlates with their superior rheological and oil-holding performance, supporting the hypothesis that increased oil content leads to tighter network packing without compromising functional integrity. This supports previous claims that high oil fraction can improve both mouthfeel and physical stability, depending on the emulsifier and drying approach used (Martínez-Velasco et al., 2024).

3.9. Spreadability assessment of oleogels

Spreadability is an essential indicator of the functional performance of semi-solid lipid systems, particularly those intended for applications such as plant-based spreads or fat substitutes. In this study, SPI–SA emulsion-templated oleogels exhibited spreadability indices ranging from 33.2 to 41.1 g·cm/s (Fig. 11), with all formulations demonstrating favorable values within the typical range for food-grade spreads (Abdallah et al., 2021). The highest spreadability was observed in the 40% (41.1 ± 0.3 g·cm/s) and 55% (39.5 ± 0.2 g·cm/s) oil content gels, which likely benefit from a looser gel network and lower resistance to deformation under applied shear. As oil content increased to 70% and 75%, spreadability values slightly decreased (33.2 and 37.4 g·cm/s, respectively), reflecting the formation of denser, more cohesive internal structures, consistent with their enhanced textural strength and rheological profiles. However, these values still fall within the acceptable spreadability range reported for oleogel-based food spreads. For comparison, Bascuas et al. (2021) reported that chocolate spreads formulated with hydrocolloid-based oleogels showed comparable consumer-accepted spreadability and sensory properties when coconut oil was partially replaced by sunflower oil-based oleogels. Likewise, Tirgarian et al. (2023) observed that water-in-oleogel emulsions used in reduced-fat chocolate spreads maintained spreadability similar to the full-fat commercial references.

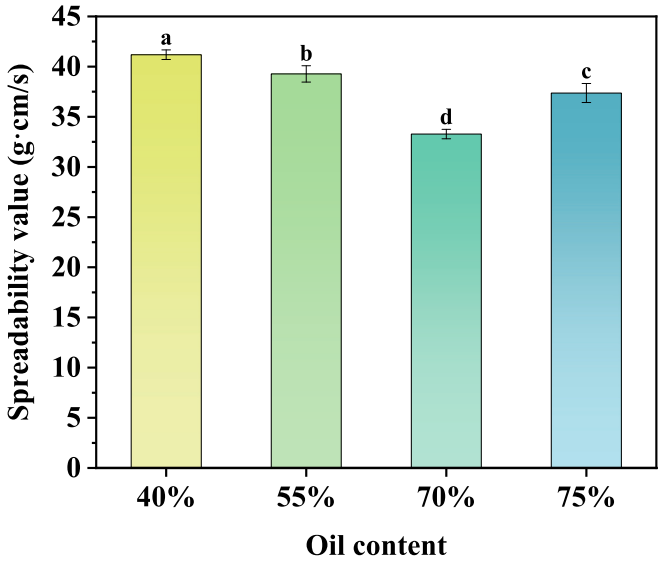

Fig. 11. Spreadability of oleogels with different oil contents. Different letters represent a significant difference ($P < 0.05$).

3.10. 3D printing accuracy and structural stability of oleogels

To evaluate the practical structuring capacity of the SPI–SA-based oleogels, their 3D printability was assessed across different oil contents (Fig. 12). Key performance indicators included dimensional accuracy, shape stability over time, and visual resolution of the printed models. Based on our printing results (Table 3), the 55% oleogel showed the highest dimensional accuracy (97.47 ± 0.51%), enabling precise layer stacking and high shape fidelity. This is consistent with previous findings where moderate-viscosity emulsions exhibit better flow control during extrusion-based printing (Qiu et al., 2023).

The 70% oleogel displayed the best shape stability over 6 h (99.10 ± 0.17%), with minimal dimensional shrinkage. This outcome is supported by its well-balanced rheological properties (high G′, low tan δ), dense microstructure, and low oil release.

Although the 75% sample demonstrated high cohesiveness and

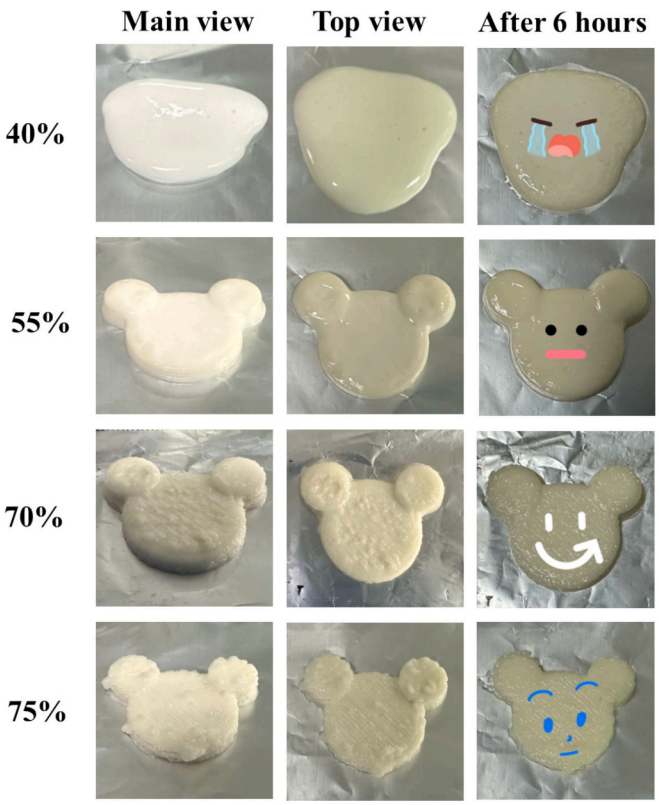

Fig. 12. Visual appearance of 3D-printed oleogels.

Table 3
Effect of oil content on the accuracy and stability of 3D printing of oleogels.

Oil content	Accuracy (%)	Stability (%)		
		2 h	4 h	6 h
55%	99.28 ± 0.14^{a}	98.87 ± 0.12^{b}	97.83 ± 0.15^{c}	96.63 ± 0.29^{c}
70%	97.47 ± 0.51^{b}	99.73 ± 0.15^{a}	99.43 ± 0.15^{a}	99.10 ± 0.17^{a}
75%	97.18 ± 0.22^{b}	99.33 ± 0.06^{c}	98.57 ± 0.12^{b}	97.93 ± 0.06^{b}

Data are presented as mean ± SD. Different superscript letters within the same column indicate significant differences between groups ($P < 0.05$).

viscoelastic strength, it exhibited slightly lower accuracy (96.90 ± 0.42%) and a rougher surface finish. This may be attributed to excessive lubrication effects caused by higher oil content, which can reduce filament fusion and increase surface irregularity during deposition. This trade-off is consistent with earlier reports showing that excessive fluidity at very high oil loadings can compromise surface smoothness and line precision (Shang et al., 2023).

Together, these results suggest a complementary relationship between oil content and 3D printing behavior: 55% gel offers superior geometric precision, 70% gel provides optimal shape retention and mechanical stability, 75% gel exhibits strong internal strength but requires flow control to ensure surface quality. This aligns with recent literature emphasizing the balance between viscoelasticity, recovery, and droplet network structure in designing oleogel-based 3D printing inks (Kan et al., 2023).

4. Conclusions

This study presents a clean-label strategy for structuring unsaturated plant oils into highly stable oleogels via emulsion-templated gelation. By utilizing glycation-enhanced SPI–SA protein–polysaccharide conjugates, we successfully constructed high internal phase emulsions with oil contents up to 78.34%, which were transformed into oleogels through mild hot-air drying. The resulting oleogels exhibited solid-like rheological behavior, excellent structural stability under ambient, thermal, and freeze–thaw conditions, and desirable functional attributes such as spreadability and 3D printability. Notably, increasing oil content enhanced the gel's oil-holding capacity and network integrity, with the 70% formulation demonstrating optimal performance in shape retention. These findings offer new insights into the design of high-oil, plant-based fat replacers and provide a promising framework for future applications in personalized nutrition, food printing, and healthy lipid structuring.

CRediT authorship contribution statement

Tao Wang: Writing – review & editing, Writing – original draft, Software, Methodology, Investigation, Formal analysis, Data curation, Conceptualization. **Manman Shi:** Writing – review & editing. **Jun Cao:** Writing – review & editing, Validation. **Pengfei Yu:** Writing – review & editing. **Fuliang Cao:** Project administration. **Erzheng Su:** Writing – review & editing, Supervision.

Declaration of competing interest

The authors declare that they have no known competing financial interests or personal relationships that could have appeared to influence the work reported in this paper.

Acknowledgment

This work was supported by the Postgraduate Research & Practice Innovation Program of Jiangsu Province (KYCX24_1340).

Data availability

Data will be made available on request.

References

Abdallah, M. H., Abu Lila, A. S., Unissa, R., Elsewedy, H. S., Elghamry, H. A., & Soliman, M. S. (2021). Preparation, characterization and evaluation of anti-inflammatory and anti-nociceptive effects of brucine-loaded nanoemulgel. *Colloids and Surfaces B: Biointerfaces, 205*, Article 111868. https://doi.org/10.1016/j.colsurfb.2021.111868

Abdolmaleki, K., Alizadeh, L., Nayebzadeh, K., Hosseini, S. M., & Shahin, R. (2020). Oleogel production based on binary and ternary mixtures of sodium caseinate, xanthan gum, and guar gum: Optimization of hydrocolloids concentration and drying method. *Journal of Texture Studies, 51*(2), 290–299. https://doi.org/10.1111/jtxs.12469

Bascuas, S., Espert, M., Llorca, E., Quiles, A., Salvador, A., & Hernando, I. (2021). Structural and sensory studies on chocolate spreads with hydrocolloid-based oleogels as a fat alternative. *LWT, 135*, Article 110228. https://doi.org/10.1016/j.lwt.2020.110228

Boonlao, N., Ruktanonchai, U. R., & Anal, A. K. (2023). Glycation of soy protein isolate with maltodextrin through Maillard reaction via dry and wet treatments and compare their techno-functional properties. *Polymer Bulletin, 80*(8), 8603–8626. https://doi.org/10.1007/s00289-022-04473-y

Cai, B., Saito, A., & Ikeda, S. (2018). Maillard Conjugation of Sodium Alginate to Whey Protein for Enhanced Resistance to Surfactant-Induced Competitive Displacement from Air–Water Interfaces. *Journal of Agricultural and Food Chemistry, 66*(3), 704–710. https://doi.org/10.1021/acs.jafc.7b04387

Carasso, M. L., Rowlands, W. N., & Kennedy, R. A. (1995). Electroacoustic determination of droplet size and zeta potential in concentrated intravenous fat emulsions. *Journal of Colloid and Interface Science, 174*(2), 405–413. https://doi.org/10.1006/jcis.1995.1408

Chen, L., & Zhang, S.-B. (2023). Structural and functional properties of self-assembled peanut protein nanoparticles prepared by ultrasonic treatment: Effects of ultrasound intensity and protein concentration. *Food Chemistry, 413*, Article 135626. https://doi.org/10.1016/j.foodchem.2023.135626

Chen, X.-W., Wang, J.-M., Guo, J., Wan, Z.-L., Yin, S.-W., & Yang, X.-Q. (2017). Hierarchical high internal phase emulsions and transparent oleogels stabilized by quillaja saponin-coated nanodroplets for color performance. *Food & Function, 8*(2), 823–831. https://doi.org/10.1039/C6FO01752E

Chen, X.-W., & Yang, X.-Q. (2019). Characterization of Orange oil powders and Oleogels fabricated from emulsion templates stabilized solely by a natural triterpene Saponin. *Journal of Agricultural and Food Chemistry, 67*(9), 2637–2646. https://doi.org/10.1021/acs.jafc.8b04588

Chen, Y., Li, S., Zhang, N., Zhang, K., & Chen, X. (2025). Development of tea polysaccharides-xanthan gum complex oleogel: Characterization and curcumin delivery. *Journal of Food Engineering, 398*, Article 112600. https://doi.org/10.1016/j.jfoodeng.2025.112600

Chen, Y., Wang, J., Xu, J., Zhang, J., Xu, S., Zhang, Q., & Gong, Z. (2023). Fabrication of a polysaccharide-protein/protein complex stabilized Oral Nanoemulsion to facilitate the therapeutic effects of 1,8-cineole on atherosclerosis. *ACS Nano, 17*(10), 9090–9109. https://doi.org/10.1021/acsnano.2c12230

Cui, X., Saleh, S. S. M., Shu, Y., Na, W., Peng, W., Minpeng, Z., & Xiao, Z. (2023). Oleogels as animal fat and shortening replacers: Research advances and application challenges. *Food Reviews International, 39*(8), 5233–5254. https://doi.org/10.1080/87559129.2022.2062769

Dinnella, C., Gargaro, M. T., Rossano, R., & Monteleone, E. (2002). Spectrophotometric assay using o-phtaldialdehyde for the determination of transglutaminase activity on casein. *Food chemistry, 78*(3), 363–368. https://doi.org/10.1016/S0308-8146(02)00109-7

Djerdjev, A. M., & Beattie, J. K. (2008). Electroacoustic and ultrasonic attenuation measurements of droplet size and ζ-potential of alkane-in-water emulsions: Effects of oil solubility and composition. *Physical Chemistry Chemical Physics, 10*(32), 4843–4852. https://doi.org/10.1039/B807623E

Erum, A., Tulain, U. R., Malik, N. S., Riaz, A., Yaqoob, M., Mahmood, A., & Tayyab, M. (2024). Formulation and optimization of pectin-based emulgel isolated from Abelmoschus esculentus using response surface methodology. *Polymer Bulletin, 81*(11), 10039–10059. https://doi.org/10.1007/s00289-024-05182-4

Hao, Z.-Z., Peng, X.-Q., & Tang, C.-H. (2020). Edible Pickering high internal phase emulsions stabilized by soy glycinin: Improvement of emulsification performance and Pickering stabilization by glycation with soy polysaccharide. *Food Hydrocolloids, 103*, Article 105672. https://doi.org/10.1016/j.foodhyd.2020.105672

Hu, S., Xiao, F., Du, M., Pan, J., Song, L., Wu, C., & Xu, X. (2023). The freeze-thaw stability of flavor high internal phase emulsion and its application to flavor preservation and 3D printing. *Food Chemistry: X, 19*, Article 100759. https://doi.org/10.1016/j.fochx.2023.100759

Hussain, A., Hussain, M., Ashraf, W., Karim, A., Muhammad Aqeel, S., Khan, A., & Lianfu, Z. (2024). Preparation, characterization and functional evaluation of soy protein isolate-peach gum conjugates prepared by wet heating Maillard reaction. *Food Research International, 192*, Article 114681. https://doi.org/10.1016/j.foodres.2024.114681

Kan, X., Dai, Z., Chen, D., Zeng, X., & Fan, X. (2023). High internal phase emulsion stabilized by whey protein isolate-gum Arabic Maillard conjugate: Characterization and application in 3D printing. *Food Hydrocolloids, 145*, Article 109137. https://doi.org/10.1016/j.foodhyd.2023.109137

Kavimughil, M., Leena, M. M., Moses, J. A., & Anandharamakrishnan, C. (2022). 3D printed MCT oleogel as a co-delivery carrier for curcumin and resveratrol. *Biomaterials, 287*, Article 121616. https://doi.org/10.1016/j.biomaterials.2022.121616

Kusumastuti, M. R., Yuliani, S., Hidayat, C., & Setiowati, A. D. (2024). Modification techno-functional properties of spirulina protein concentrates (Arthrospira Platensis) as O/W emulsifier by conjugation and electrostatic complexations. *Innovative Food Science & Emerging Technologies, 95*, Article 103727. https://doi.org/10.1016/j.ifset.2024.103727

Kutzli, I., Gibis, M., Baier, S. K., & Weiss, J. (2018). Formation of whey protein isolate (WPI)–maltodextrin conjugates in fibers produced by needleless electrospinning. *Journal of Agricultural and Food Chemistry, 66*(39), 10283–10291. https://doi.org/10.1021/acs.jafc.8b02104

Leahu, A., Ghinea, C., Ropciuc, S., & Damian, C. (2025). Textural, color, and sensory analysis of cookies prepared with hemp oil-based Oleogels. *Gels, 11*(1), 46. https://doi.org/10.3390/gels11010046

Leng, X., Cheng, S., Wu, H., Nian, Y., Zeng, X., & Hu, B. (2022). High internal phase emulsions stabilized with polyphenol-amyloid fibril Supramolecules for encapsulation and protection of lutein. *Journal of Agricultural and Food Chemistry, 70*(7), 2328–2338. https://doi.org/10.1021/acs.jafc.1c04615

Lertittikul, W., Benjakul, S., & Tanaka, M. (2007). Characteristics and antioxidative activity of Maillard reaction products from a porcine plasma protein-glucose model system as influenced by pH. *Food Chemistry, 100*(2), 669–677. https://doi.org/10.1016/j.foodchem.2005.09.085

Li, C., Su, S., Li, H., Qin, S., Wu, Y., Ouyang, K., & Zeng, C. (2025). High internal phase Pickering emulsions stabilized by natural deep eutectic solvents: The freeze-thaw stability and cryopreservation capability. *LWT, 215*, Article 117193. https://doi.org/10.1016/j.lwt.2024.117193

Li, L., Huang, Y., Ding, Q., Wang, D., Yuan, T., Song, G., & Gong, J. (2025). Formation and functional improvement of α-casein, β-lactoglobulin, and hyaluronic acid conjugates via the Maillard reaction: Comparison with different mass ratios. *Food Chemistry, 475*, Article 143322. https://doi.org/10.1016/j.foodchem.2025.143322

Li, L., Liu, G., Bogojevic, O., Pedersen, J. N., & Guo, Z. (2022). Edible oleogels as solid fat alternatives: Composition and oleogelation mechanism implications. *Comprehensive Reviews in Food Science and Food Safety, 21*(3), 2077–2104. https://doi.org/10.1111/1541-4337.12928

Ling, M., Huang, X., He, C., & Zhou, Z. (2024). Tunable rheological properties of high internal phase emulsions stabilized by phosphorylated walnut protein/pectin complexes: The effects of pH conditions, mass ratios, and concentrations. *Food Research International, 175*, Article 113670. https://doi.org/10.1016/j.foodres.2023.113670

Ma, X., Chi, C., Pu, Y., Miao, S., & Liu, D. (2022). Conjugation of soy protein isolate (SPI) with pectin: Effects of structural modification of the grafting polysaccharide. *Food Chemistry, 387*, Article 132876. https://doi.org/10.1016/j.foodchem.2022.132876

Manzoor, S., Masoodi, F. A., Naqash, F., & Rashid, R. (2022). Oleogels: Promising alternatives to solid fats for food applications. *Food Hydrocolloids for Health, 2*, Article 100058. https://doi.org/10.1016/j.fhfh.2022.100058

Martínez-Velasco, A., Trujillo-Ramírez, D., Bustos-Vázquez, G., & Cervantes-Arista, C. (2024). The use of candelilla wax/canola oil oleogel in the formulation of sponge cake bread improves morphostructural and sensory properties. *Discover Food, 4*(1), 160. https://doi.org/10.1007/s44187-024-00245-x

Miao, W., Zhang, Z., Lin, Q., McClements, D. J., Ji, H., Jiang, L., & Qiu, C. (2025). Preparation of emulsion-template oleogels: Tuning properties by controlling initial water content and evaporation method. *Food Hydrocolloids, 158*, Article 110519. https://doi.org/10.1016/j.foodhyd.2024.110519

Moradabbasi, M., Goli, S. A. H., & Fayaz, G. (2022). Effect of biopolymers concentration and drying methods on physicochemical properties of emulsion-templated oleogel. *Journal of Food Science and Technology, 59*(5), 1994–2003. https://doi.org/10.1007/s13197-021-05214-1

Morales, E., Iturra, N., Contardo, I., Quilaqueo, M., Franco, D., & Rubilar, M. (2023). Fat replacers based on oleogelation of beeswax/shellac wax and healthy vegetable oils. *LWT, 185*, Article 115144. https://doi.org/10.1016/j.lwt.2023.115144

Onaizi, S. A. (2022). Effect of oil/water ratio on rheological behavior, droplet size, zeta potential, long-term stability, and acid-induced demulsification of crude oil/water nanoemulsions. *Journal of Petroleum Science and Engineering, 209*, Article 109857. https://doi.org/10.1016/j.petrol.2021.109857

Pal, R. (2006). Rheology of high internal phase ratio emulsions. *Food Hydrocolloids, 20*(7), 997–1005. https://doi.org/10.1016/j.foodhyd.2005.12.001

Palla, C., Giacomozzi, A., Genovese, D. B., & Carrín, M. E. (2017). Multi–objective optimization of high oleic sunflower oil and monoglycerides oleogels: Searching for rheological and textural properties similar to margarine. *Food Structure, 12*, 1–14. https://doi.org/10.1016/j.foostr.2017.02.005

Pan, H., Xu, X., Qian, Z., Cheng, H., Shen, X., Chen, S., & Ye, X. (2021). Xanthan gum-assisted fabrication of stable emulsion-based oleogel structured with gelatin and proanthocyanidins. *Food Hydrocolloids, 115*, Article 106596. https://doi.org/10.1016/j.foodhyd.2021.106596

Pan, L., Li, Z., Liu, J., Geng, T., Liu, X., Dong, D., & Liu, H. (2025). Fabrication of oil-in-water high internal phase emulsions with enhanced antioxidative properties by modified starch/polyphenol mixtures: Effect of EGCG concentration, NaCl concentration, and temperature. *International Journal of Biological Macromolecules, 295*, Article 139585. https://doi.org/10.1016/j.ijbiomac.2025.139585

Peng, X.-Q., Xu, Y.-T., Liu, T.-X., & Tang, C.-H. (2018). Molecular mechanism for improving emulsification efficiency of soy Glycinin by glycation with soy soluble polysaccharide. *Journal of Agricultural and Food Chemistry, 66*(46), 12316–12326. https://doi.org/10.1021/acs.jafc.8b03398

Plazzotta, S., Calligaris, S., & Manzocco, L. (2020). Structural characterization of oleogels from whey protein aerogel particles. *Food Research International, 132*, Article 109099. https://doi.org/10.1016/j.foodres.2020.109099

Qiu, C., Wang, C., Li, X., Sang, S., McClements, D. J., Chen, L., & Jin, Z. (2023). Preparation of high internal phase Pickering emulsion gels stabilized by glycyrrhizic acid-zein composite nanoparticles: Gelation mechanism and 3D printing performance. *Food Hydrocolloids, 135*, Article 108128. https://doi.org/10.1016/j.foodhyd.2022.108128

Roland, I., Piel, G., Delattre, L., & Evrard, B. (2003). Systematic characterization of oil-in-water emulsions for formulation design. *International Journal of Pharmaceutics, 263*(1), 85–94. https://doi.org/10.1016/S0378-5173(03)00364-8

Shang, W., Sun, Y., Song, J., Zhang, P., Hou, Y., Wang, H., & Tan, M. (2023). Novel high internal phase oleogels-in-water Pickering emulsions stabilized solely by whey protein isolate for 3D printing and fucoxanthin delivery. *Food Hydrocolloids, 140*, Article 108609. https://doi.org/10.1016/j.foodhyd.2023.108609

Shuai, X., McClements, D. J., Geng, Q., Dai, T., Ruan, R., Du, L., & Chen, J. (2023). Macadamia oil-based oleogels as cocoa butter alternatives: Physical properties, oxidative stability, lipolysis, and application. *Food Research International, 172*, Article 113098. https://doi.org/10.1016/j.foodres.2023.113098

Sun, X., Cui, Q., Li, R., Hao, L., Liu, H., Wang, X., & Zhao, X. (2022). Structural and emulsifying properties of soybean protein isolate glycated with glucose based on pH treatment. *Journal of the Science of Food and Agriculture, 102*(11), 4462–4472. https://doi.org/10.1002/jsfa.11800

Sun, Y., Ma, S., Liu, Y., Jia, Z., Li, X., Liu, L., & Jiang, S. (2023). Changes in interfacial composition and structure of milk fat globules are crucial regulating lipid digestion in simulated in-vitro infant gastrointestinal digestion. *Food Hydrocolloids, 134*, Article 108003. https://doi.org/10.1016/j.foodhyd.2022.108003

Tan, Z., Yang, X., Wang, Z., Chen, Z., Pan, J., Sun, Q., & Dong, X. (2024). Konjac glucomannan-assisted fabrication of stable emulsion-based oleogels constructed with pea protein isolate and its application in surimi gels. *Food Chemistry, 443*, Article 138538. https://doi.org/10.1016/j.foodchem.2024.138538

Tao, L., Wang, H., Wang, J., Zhang, J., Yu, L., & Song, S. (2024). Characterization and emulsion stability of soybean protein isolate/soybean peptide and ginseng polysaccharide conjugates. *LWT, 196*, Article 115860. https://doi.org/10.1016/j.lwt.2024.115860

Tirgarian, B., Yadegari, H., Bagheri, A., Neshagaran, E., Mardani, M., & Farmani, J. (2023). Reduced-fat chocolate spreads developed by water-in-oleogel emulsions. *Journal of Food Engineering, 337*, Article 111233. https://doi.org/10.1016/j.jfoodeng.2022.111233

Tripathi, S., Bhattacharya, A., Singh, R., & Tabor, R. F. (2017). Rheological behavior of high internal phase water-in-oil emulsions: Effects of droplet size, phase mass fractions, salt concentration and aging. *Chemical Engineering Science, 174*, 290–301. https://doi.org/10.1016/j.ces.2017.09.016

Wang, M., Huang, S., Fan, L., & Li, J. (2023). All-natural gel-in-gel water-in-oil high internal phase emulsions featuring biphasic network stabilization and application of

3D printing. *Colloids and Surfaces A: Physicochemical and Engineering Aspects, 678*, Article 132529. https://doi.org/10.1016/j.colsurfa.2023.132529
Wang, Q., Espert, M., Flores, M., Sanz, T., & Salvador, A. (2025). Oxidative and texture storage stability of HPMC sunflower oil oleogels prepared by different indirect approaches. *Food Hydrocolloids, 164*, Article 111158. https://doi.org/10.1016/j.foodhyd.2025.111158
Wang, Y., Yu, J., Xu, N., Wang, G., & Wang, X. (2019). Influence of protein hydrolysis on the freeze-thaw stability of emulsions prepared with soy protein - dextran conjugates. *Journal of Oleo Science, 68*(10), 959–965. https://doi.org/10.5650/jos.ess19076
Wang, Z., Jayani, C., Tuyen, T., & Farahnaky, A. (2023). Oleogels prepared with low molecular weight gelators: Texture, rheology and sensory properties, a review. *Critical Reviews in Food Science and Nutrition, 63*(23), 6069–6113. https://doi.org/10.1080/10408398.2022.2027339
Wang, Z., Zhao, Y., Liu, H., Chen, Q., Liu, Q., & Kong, B. (2024). Soy protein isolate-sodium alginate colloidal particles for improving the stability of high internal phase Pickering emulsions: Effects of mass ratios. *Food Chemistry: X, 21*, Article 101094. https://doi.org/10.1016/j.fochx.2023.101094
Welch, C. F., Rose, G. D., Malotky, D., & Eckersley, S. T. (2006). Rheology of high internal phase emulsions. *Langmuir, 22*(4), 1544–1550. https://doi.org/10.1021/la052207h
Xie, F., Ren, X., Zhu, Z., Luo, J., Zhang, H., Xiong, Z., & Ai, L. (2023). Tamarind seed polysaccharide-assisted fabrication of stable emulsion-based oleogel structured with gelatin: Preparation, interaction, characterization, and application. *Food Hydrocolloids, 142*, Article 108761. https://doi.org/10.1016/j.foodhyd.2023.108761
Xu, X., Fan, L., & Li, J. (2024). Freeze–thaw stability of high-internal-phase emulsion stabilized by chickpea protein microgel particles and its application in surimi. *Journal of the Science of Food and Agriculture, 104*(14), 8621–8633. https://doi.org/10.1002/jsfa.13690
Yi, J., Chen, X., Wen, Z., & Fan, Y. (2024). Improving the functionality of pea protein with laccase-catalyzed crosslinking mediated by chlorogenic acid. *Food Chemistry, 433*, Article 137344. https://doi.org/10.1016/j.foodchem.2023.137344
Zhang, D., Zhang, Y., Huang, Y., Chen, L., Bao, P., Fang, H., & Zhou, C. (2021). L-arginine and l-lysine alleviate myosin from oxidation: Their role in maintaining myosin's emulsifying properties. *Journal of Agricultural and Food Chemistry, 69*(10), 3189–3198. https://doi.org/10.1021/acs.jafc.0c06095
Zhang, R., Cheng, L., Luo, L., Hemar, Y., & Yang, Z. (2021). Formation and characterisation of high-internal-phase emulsions stabilised by high-pressure homogenised quinoa protein isolate. *Colloids and Surfaces A: Physicochemical and Engineering Aspects, 631*, Article 127688. https://doi.org/10.1016/j.colsurfa.2021.127688
Zhang, R., Mu, Z., Xu, H., Yang, N., Bilawal, A., Jiang, Z., & Hou, J. (2024). Insight into sequential extrusion and cysteine treatment for improving rheological characteristics and in vitro digestibility of whey protein isolate. *Journal of Agricultural and Food Chemistry, 72*(47), 26514–26523. https://doi.org/10.1021/acs.jafc.4c07574
Zhang, Y., Lu, Y., Zhang, R., Gao, Y., & Mao, L. (2021). Novel high internal phase emulsions with gelled oil phase: Preparation, characterization and stability evaluation. *Food Hydrocolloids, 121*, Article 106995. https://doi.org/10.1016/j.foodhyd.2021.106995
Zhang, Y., Wang, Y., Zhang, R., Yu, J., Gao, Y., & Mao, L. (2022). Tuning the rheological and tribological properties to simulate oral processing of novel high internal phase oleogel-in-water emulsions. *Food Hydrocolloids, 131*, Article 107757. https://doi.org/10.1016/j.foodhyd.2022.107757
Zheng, S., Lu, M., Xiao, J., Zhang, X., Li, J., Zhang, H., & Lan, Y. (2023). A novel strategy for preparation of rice bran protein oleogels based on high internal phase emulsion template. *Journal of the Science of Food and Agriculture, 103*(12), 5717–5726. https://doi.org/10.1002/jsfa.12672
Zhu, W.-W., Zhang, Y., & Tang, C.-H. (2023). Maximizing cholesterol-lowering benefits of soy protein isolate by glycation with soy soluble polysaccharide. *Food Hydrocolloids, 135*, Article 108131. https://doi.org/10.1016/j.foodhyd.2022.108131
Zou, Y., Yang, X., & Scholten, E. (2019). Tuning particle properties to control rheological behavior of high internal phase emulsion gels stabilized by zein/tannic acid complex particles. *Food Hydrocolloids, 89*, 163–170. https://doi.org/10.1016/j.foodhyd.2018.10.037